Chemical Science

ROYAL SOCIETY OF CHEMISTRY

EDGE ARTICLE

View Article Online
View Journal

Cite this: DOI: 10.1039/d5sc08665e

All publication charges for this article have been paid for by the Royal Society of Chemistry

Received 7th November 2025
Accepted 21st December 2025

DOI: 10.1039/d5sc08665e

rsc.li/chemical-science

Single-cell structural lipidomics using a miniature dual-LIT mass spectrometer

Zhijun Cai, Ningxi Li, Simin Cheng, Zheng Ouyang* and Xiaoxiao Ma *

Structural lipidomics provides comprehensive information on lipidomes, and there is great interest in applying it to single-cell analysis for accurate cell phenotyping and lipid pathway studies. However, structural lipidomics relies on tandem mass spectrometry analysis of a large number of lipid species, which remains challenging for single-cell analysis due to the small sample amounts. Herein, using a miniature dual-linear ion trap (LIT) mass spectrometer with enhanced ion processing capability, we developed an effective strategy to achieve annotations of more than 100 lipid species in a single cell with high structural specificity. The ion utilization efficiency was greatly improved with multi-stage MS^n (n = 2–4) analysis performed for each lipid species to acquire structural information at different levels. From a single MDA-MB-468 cancer cell, we identified 100+ lipids, including 64 lipids at the acyl-chain sum composition level, 23 at the *sn*-position level, 30 at the C=C location level, and 20 at the C=C/*sn*-position level, primarily phosphatidylcholamines (PCs) and phosphatidylethanolamines (PEs). Significant variations in *sn*-position and C=C location isomers were observed in doxorubicin-resistant and -sensitive K562 cells. With enriched information at the structural lipidomics level, the correlation was established between variations in lipidome and response to ferroptosis for human cancer cells.

Introduction

Single-cell analysis has enabled and accelerated studies of cell-to-cell heterogeneities that are instrumental in understanding disease development.[1–4] The technical advancement and applications of single-cell genomics, transcriptomics, and proteomics have made significant contributions to biological science. Lipidomics is an essential part of metabolomics that is also expected to provide important information regarding the biological processes of a single cell.[5–9] Lipids serve as crucial cellular metabolites, constituting integral components of membranes and organelles and playing pivotal roles in processes such as cell division, endocytosis, protein export, and cell signaling.[10–12] The combination of lipidomics with other omics methods applied to single-cell studies has contributed to the understanding of the genetic and molecular basis of diseases, molecular changes that occur during the development of organisms, and the immune system's response to infections.[13,14] Mass spectrometry (MS) is the most effective tool for lipidomics due to its exceptional structural characterization capability.

In the past decade, powerful lipid structural characterization tools have emerged that have unraveled the complexity of the human lipidome, in particular at the C=C location/geometry and fatty acyl *sn*-position levels.[15–17] These tools rely on tandem MS (MS/MS or MS^n) analysis, and were also shown to be effective in combination with chemical derivatization,[18,19] such as for PB-MS/MS (PB, Paternò–Büchi reaction[20]). Consequently, these technical advancements also led to the consensus that the field of lipidomics has entered the era of structural lipidomics. Alternative lipid metabolic pathways have been revealed,[21,22] and potential disease biomarkers have been proposed,[23,24] which are critical for understanding diseases and finding new therapeutic targets.

The application of structural lipidomic technologies for single-cell analysis, however, faces significant challenges stemming from the limited sample availability of a single cell, especially for mammalian cells.[25] Conventional mass spectrometers with MS/MS capabilities are mostly designed for coupling with liquid chromatography, where ions from a sample are not utilized at high efficiency when MS/MS analysis is performed. Using a commercial ion trap, triple-quadrupole, or quadrupole-time-of-flight (TOF) mass spectrometers as an example, ions of only one target precursor are used for each MS/MS scan, with all the others wasted.[26] The consequence of using these instruments for single-cell structural lipidomics analysis is low coverage of lipid species that can be identified with a high level of structural confidence.

Numerous methods have been explored to address these limitations for single-cell analysis. Qin *et al.* developed ID-organic cytoMS, incorporating an efficient online lysis system that extended single-cell analysis time from seconds to tens of

State Key Laboratory of Precision Measurement Technology and Instruments, Department of Precision Instruments, Tsinghua University, Beijing 100084, China. E-mail: ouyang@mail.tsinghua.edu.cn; maxx@mail.tsinghua.edu.cn

seconds.[27] This approach enabled the identification of 150 metabolite species from a single MCF-7 cancer cell, although the number of identified lipid species remained lower, likely due to sample dilution during analysis. The Li group extended trapped ion mobility separation to dual-polarity ionization mass spectrometry imaging for *in situ* single-cell lipidomics analysis. With this method, it was revealed that a total of 185 lipids were derived from single cells,[28] but lipids are identified at the lipid sum composition level without in-depth structural information such as C=C location and *sn*-positions of fatty acyls. We explored the combination of on-demand nano-electrospray ionization (nanoESI) with photochemical derivatization using the PB reaction,[29] empowering single-cell lipid analysis with C=C location specificity. However, the coverage of the lipid species was still limited by the number of MS/MS analyses and ultimately the sample amount from a single cell.

To truly apply structural lipidomics for single-cell analysis, it is highly desirable to increase the coverage of the lipid species from a single cell, which indicates that MS^n analysis with significantly improved efficiency for sample usage is required. It should be noted that MS^3 or MS^4 might also be required for comprehensive lipid structural characterization. For instance, determining the C=C location in an *sn*-specific fatty acyl requires two rounds (*sn*-1 and *sn*-2) of MS^4 analysis for ultimate structure determination.[30,31]

With these considerations, we explored the development of a high-coverage single-cell structural lipidomics method utilizing a miniature dual-linear ion trap (LIT) mass spectrometer.[32,33] Ions were stored in LIT 1 and could be partially, mass-selectively transferred to LIT 2 for MS^n (n = 2–4) analysis. That facilitated the comprehensive and targeted interrogation of the lipidome. The single-cell structural lipidomics approach enabled the identification of approximately 100 lipids from a single MDA-MB-468 breast cancer cell, including the precise determination of C=C locations in *sn*-specific fatty acyls of phospholipids, representing the most in-depth characterization of phospholipids within single cells to date. Although our method is highly effective for PCs and PEs, its application to other lipid classes may require further optimization.

We successfully applied the method to distinguish between doxorubicin (DOX)-resistant and DOX-sensitive human chronic myelogenous leukemia (CML) K562 cells based on their unique lipidomic profiles, leveraging the quantitative information obtained at the C=C location and *sn*-position levels. We also evaluated the erastin-induced ferroptosis in human breast and liver cancer cell lines and uncovered a transition state between normal and ferroptotic cells. These findings underscore the significant potential of this novel single-cell structural lipidomics method for advancing the understanding of cellular heterogeneity.

Results and discussion

The single-cell MS platform based on dual-LIT MS

The platform integrated the single-cell ion source with the dual-LIT MS platform (Fig. 1a). The single-cell sampling and ionization method was modified from the reported methods that involved cell fixation, migration, derivatization, and ionization.[29] The optimized workflow is shown in Fig. S1a and comprises three steps. Step 1: single cells were suspended in a methanol/H_2O mixture (1 : 1, v/v) and migrated to the capillary tip *via* gravity, followed by drying. This solvent condition was chosen to minimize lipid dissolution in the solvent and promote on-demand ionization for sensitive analysis. Step 2: lipids were derivatized using 2-acetylpyridine (2-AP, 121.14 g mol^{-1}) in acetonitrile/water (1 : 1, v/v) *via* a droplet-assisted method. Step 3: lipids were ionized using on-demand nanoESI with methanol/acetonitrile (1 : 1, v/v) containing 1% formic acid.[34] This gravity-based cell migration method, different from electro-migration, enabled parallel processing of multiple cells (>100) with an average processing time of less than 10 s per cell. Furthermore, the methanol/H_2O-based cell suspension method eliminated the need for glutaraldehyde fixation, preserving crucial phospholipid species such as PEs (Fig. S1c). To ensure optimal performance, the time for matching the single-cell ion source with dual-LIT MS was carefully optimized (Fig. S2). However, the round of sampling from a single cell using on-demand nanoESI was limited to four, which was fewer than achievable with glutaraldehyde fixation methods,[29] as shown in Fig. S3. This limitation might be attributed to potential lipid loss during the methanol/H_2O-based cell suspension process.

The dual-LIT MS system, described in detail in the 'Dual-LIT MS System' section of the SI, played a crucial role in this study. Ionized lipids from single cells were trapped in LIT 1 and mass-selectively transferred to LIT 2 for MS^n (n = 2–4) analysis (Fig. 1a). Optimization of the dual-LIT MS system, particularly the vacuum regulation system (Fig. S4a), significantly enhanced ion transfer efficiency and storage time, leading to improved sensitivity and enabling multiple ion analysis capabilities.[35] Notably, dual-LIT MS efficiently stored ions for more than 30 s with minimal ion loss (<10%) (Fig. S4b–d), and therefore, it is well-suited for single-cell lipidomics by maximizing ion utilization. This platform also offers versatile MS^n capabilities tailored for comprehensive lipid structure characterization.

Three unique operational modes were employed in this work (Fig. 1b): (i) mass-selective axial transfer (MSAT), enabling sequential and selective ion transfer from LIT 1 to LIT 2 for efficient multiple MS/MS analyses with high ion utilization;[33] (ii) multiple mass-selective partial transfers (MMPTs), facilitating the transfer of ions of a specific m/z in multiple batches to acquire detailed structural information at various levels; (iii) selective accumulation of low-abundance ions, which enhanced the detection of low-abundance ions by accumulating them in LIT 1 *via* ejecting high-abundance ions. The MMPT was developed based on the MSAT method. MSAT utilized an AC signal with a sufficiently large amplitude to efficiently transfer ions from LIT 1 to LIT 2. By reducing the AC amplitude, only a portion of the ions was transferred (Fig. S5). This principle formed the basis of MMPTs, where partial ion transmission was repeated multiple times until all ions of a target lipid were transferred for subsequent MS^n analysis (Fig. S6 and 7).

The dual-LIT MS platform features unique ion manipulation capabilities, including the ability to perform MS^n analysis and three operational modes. Leveraging the optimized vacuum

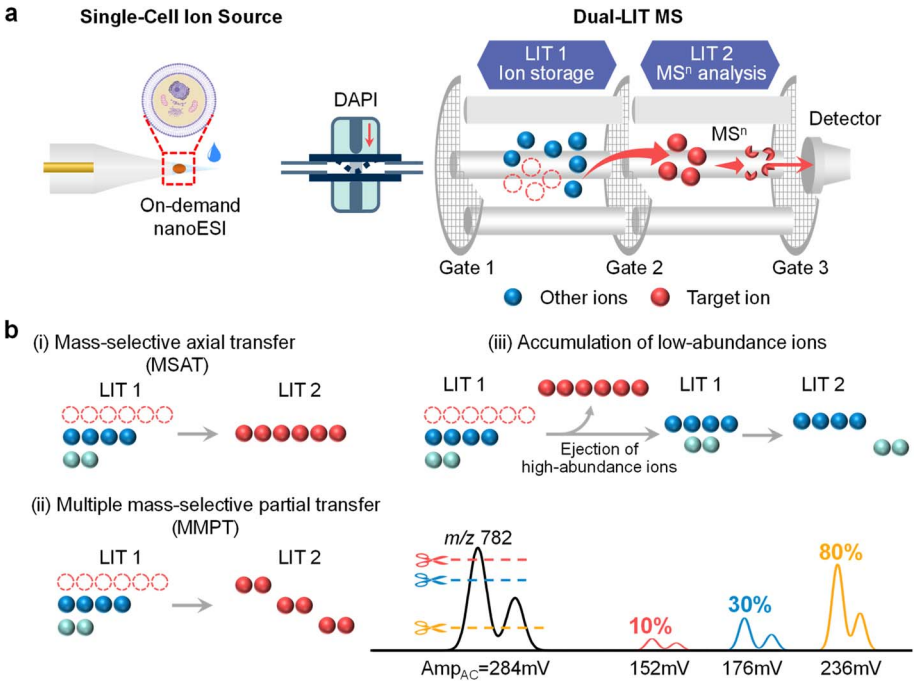

Fig. 1 The dual-LIT-MS platform for single-cell structure lipidomics, and its operational modes for lipid transfer and tandem MS analysis. (a) The platform of single-cell MS based on dual-linear ion trap mass spectrometry (dual-LIT MS). DAPI: discontinuous atmospheric pressure interface. (b) Three modes of dual-LIT MS: (i) mass-selective axial transfer (MSAT) between LIT 1 and LIT 2, (ii) multiple mass-selective partial transfer (MMPT) between LIT 1 and LIT 2, and (iii) selective accumulation of low-abundance ions.

system, the platform exhibits exceptional ion storage capacity, maximizing ion utilization. In conjunction with optimized single-cell sampling and ionization methods, this integrated single-cell MS platform enables comprehensive and detailed lipid structural characterization at the omics level. The lipid structures characterized include lipid acyl-chain sum compositions, C=C locations, *sn*-positions of fatty acyl, and C=C locations in *sn*-specific fatty acyl (C=C/*sn*-position).

High coverage lipid analysis with C=C location specificity

The dual-LIT mass spectrometer can maximize ion utilization due to its excellent ion storage capability. However, achieving high-coverage lipid profiling within single cells remains challenging. During MSAT, high-abundance ions could interfere with the transmission of low-abundance ions, particularly those with *m*/*z* values differing by only 2 Da, as evidenced in Fig. S8. Simulation studies, detailed in the 'Theoretical model and simulation method' section of the SI, elucidated the mechanism of the interference. When only target ions (blue) were present in the ion trap, they exhibited stable motion (Fig. 2b and c). However, the introduction of high-abundance interfering ions (red) disrupted this stability (Fig. 2d and e).

Analysis of ion movement frequencies revealed that the resonance point of the target ion was shifted towards the resonance point of the interfering ion (Fig. 2f). The frequency shift could be attributed to the collective interactions of ions, also known as the space-charge effect.[36,37] The inherent characteristics of cellular lipidomes further exacerbated the interference between different ions. On the one hand, lipid ion abundances within a single cell could span several orders of magnitude. On the other hand, the presence of phospholipids with varying degrees of unsaturation resulted in closely spaced *m*/*z* values, often differing by only 2 Da, which significantly complicates ion isolation and transmission.

To enhance the dynamic range for lipid detection, a targeted lipidomic strategy was developed, as illustrated in Fig. 2a, to enable high coverage and C=C structural specificity of lipid analysis within single cells. This strategy, implemented on the single-cell MS platform, involved the separate analysis of high- and low-abundance lipid ions to maximize single-cell lipidome coverage. Low-abundance ions were selectively accumulated in LIT 1, utilizing mode (iii) depicted in Fig. 1b, and subjected to multiple rounds of MS/MS. In contrast, high-abundance ions were analyzed following a separate ion injection. Accumulation of low-abundance ions was achieved using a stored waveform inverse Fourier transform (SWIFT) waveform.[38,39] The SWIFT waveform, a short-duration (approximately 35 ms) broadband voltage signal (Fig. 2j), efficiently isolated ions of specific *m*/*z* values from a complex mixture. Secular frequencies of ions to be stored in LIT 1 were selectively excluded from the SWIFT waveform, resulting in 'notches' in the frequency spectrum (Fig. 2k). Of note, the average time required for ion isolation using SWIFT (radial ejection) was significantly shorter (<1 ms) than using axial ejection (MSAT) due to the considerably smaller radial dimension of the LIT compared to its axial length.

To implement the targeted lipidomics strategy outlined in Fig. 2a, it was necessary to first identify the target peaks for MS/

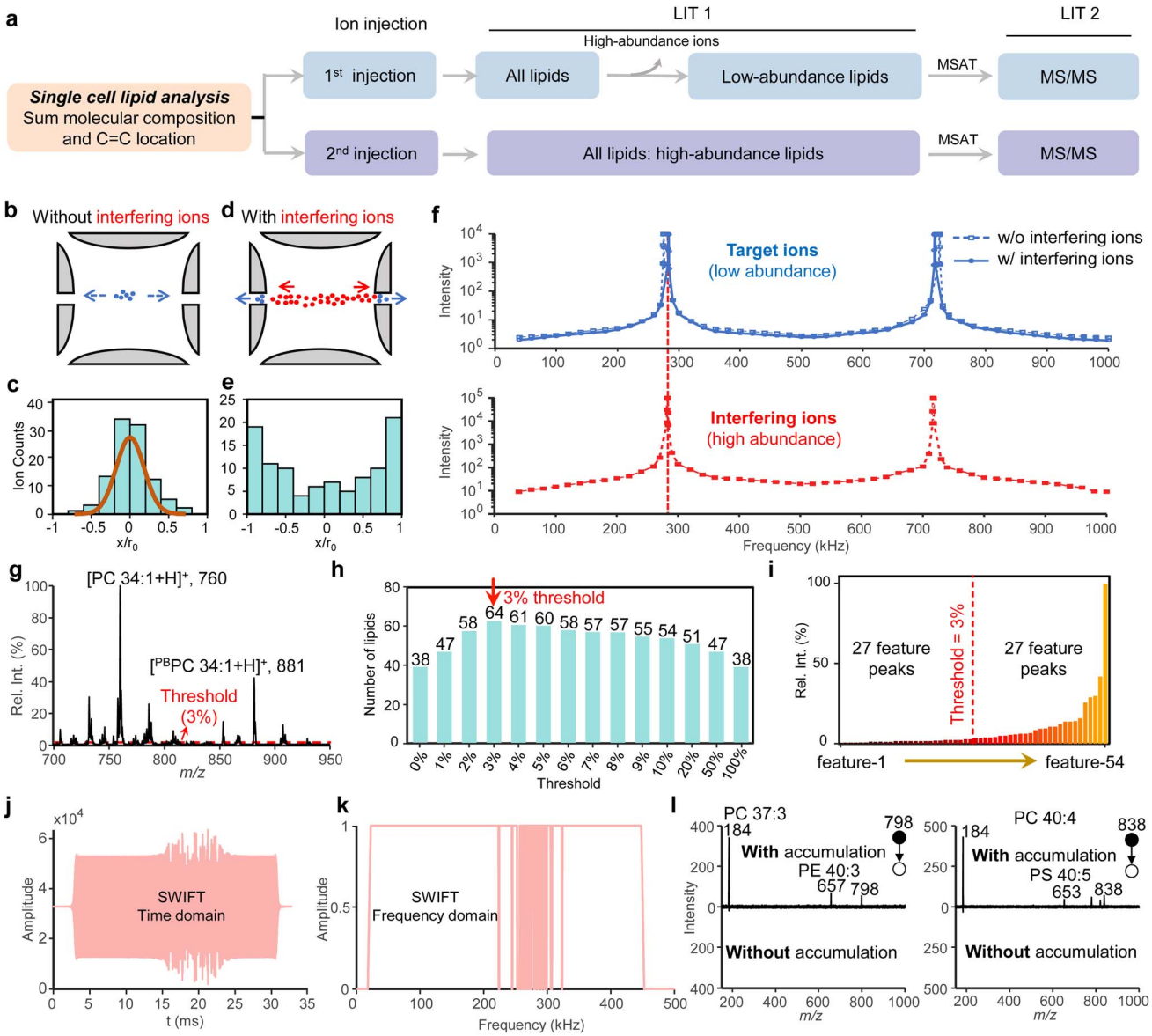

Fig. 2 Lipid structure identification at the level of sum composition and C=C location for a single MDA-MB-468 cell. (a) Workflow of single-cell structural lipidomics at the level of sum composition and C=C location. (b–f) Simulation of ion interference. Target ions (blue, *m/z* 760): 100 simulated ions used to represent 1×10^4 real ions. Interfering ions (red, *m/z* 758): 1000 simulated ions used to represent 1×10^5 real ions. (b) Target ions in the ion trap without interfering ions, and (c) distribution of target ions in the ion trap. (d) Target ions in the ion trap with interfering ions, and (e) distribution of target ions in the ion trap. (f) Simulated ion intensities as a function of applied AC frequencies. The upper part represents the simulated ion intensity of the target ions, without interfering ions (dotted line) and with interfering ions (solid line). The lower part represents the simulated ion intensity of the interfering ions. (g–i) The threshold determination for distinguishing low-abundance ions from high-abundance ions. (g) MS spectrum. (h) Number of identified lipid compositions for different thresholds, and (i) distribution of high- and low-abundance ions. (j and k) Wave of stored waveform inverse Fourier transform (SWIFT) for single MDA-MB-468 cells. (j) Wave in the time domain, and (k) wave in the frequency domain. (l) MS/MS spectra to determine lipid type with accumulation and without accumulation for *m/z* 798 and *m/z* 838.

MS analysis. A typical single-cell MS1 spectrum following PB reaction is shown in Fig. 2g. By repeatedly collecting lipid MS1 data from 10 single cells, 54 stable mass spectral features were identified for MDA-MB-468 cells (Fig. S9). Subsequently, the threshold for distinguishing high- and low-abundance ions was optimized. During the optimization process, 0.5 μL of cellular extracts in methanol/acetonitrile (1 : 1, v/v) was transferred to the nanoESI capillary to test repeatability. Lipids that were successfully identified in three replicate analyses were considered for further investigation. As illustrated in Fig. 2h, a 3% relative intensity (Rel. Int. (%)) threshold was determined to be the optimal threshold for distinguishing low-abundance ions from high-abundance ions. It should be noted that the 3% relative intensity threshold for distinguishing high- and low-abundance ions was optimized using the MDA-MB-468 cell line. While this threshold was also applicable to the MCF-7 and BT-474 breast cancer cells analyzed in this study, its universality may be limited for cell types with vastly different lipid

compositions, and re-optimization would be necessary for such applications.

In this study, we employed a relative quantification method, which was straightforward for quantifying the relative amounts of lipid isomers. Fig. 2i shows the distribution of high- and low-abundance ions. For the MDA-MB-468 cell, 27 low-abundance and 27 high-abundance lipid ions were detected. In particular, the SWIFT waveform (Fig. 2j and k) was generated according to the identified low-abundance feature peaks. The isolation efficiency of lipid targets using the SWIFT waveform exceeded 85%, as demonstrated in Fig. S10.

Following the establishment of the analysis strategy, multiple single cells were analyzed. The gas pressure curves for analyzing high- and low-abundance ions are presented in Fig. S11. The time for an injection was 100 ms, and an MSAT was 50 ms. Each MS/MS analysis required 900 ms for data acquisition. Consequently, the total analysis time for low- and high-abundance ions was approximately 50 s. The efficacy of ion accumulation was demonstrated by comparing MS/MS spectra of some specific low-abundance ions with and without accumulation (Fig. 2l). An improvement greater than 10-fold in the signal-to-noise (S/N) ratios of lipids was observed. This enhanced sensitivity enabled the identification of previously undetectable lipids, including PC 37:3, PE 40:3, PC 40:4, and PS 40:5, based on the presence of their characteristic fragment ions.

Among the 54 feature peaks identified in MDA-MB-468 cells, 9 were PB product ions, including ^{PB}PC 32:1, ^{PB}PC 34:2, ^{PB}PC 34:1, ^{PB}PC 36:3, ^{PB}PC 36:2, ^{PB}PC 36:1, ^{PB}PC 38:4, ^{PB}PE 36:2, and ^{PB}PE 36:1. By analyzing these PB product ions *via* MS/MS, the C=C location of lipids can be determined. This is achieved through a single-cell online PB reaction process, which is illustrated in Fig. 3a and consists of five steps, all completed within approximately 1 minute: (1) single-cell migration to the capillary tip; (2) application of 10 mmol L^{-1} 2-AP in acetonitrile/H_2O (v/v, 1 : 1); (3) 254 nm UV irradiation for 30 s; (4) solvent evaporation; (5) on-demand nanoESI analysis. Diagnostic ions for C=C locations at *n*-10, *n*-9, and *n*-7 locations were detected in the MS/MS spectra of ^{PB}PC 32:1 and ^{PB}PE 36:1 (Fig. 3b and c). Additional MS/MS spectra of these PB product ions are presented in Fig. S13 and S14.

All MS/MS spectra of the 54 feature peaks observed in the MDA-MB-468 cell are shown in Fig. S15. Peaks with an S/N ratio of >3 in the MS/MS spectra were considered for subsequent analysis. Lipid acyl-chain sum compositions and C=C locations were determined based on the characteristic fragment ions generated during MS/MS analysis. For instance, after CID PCs generate characteristic fragments at *m*/*z* 184, PEs exhibit a characteristic neutral loss of 141 Da, and PSs exhibit

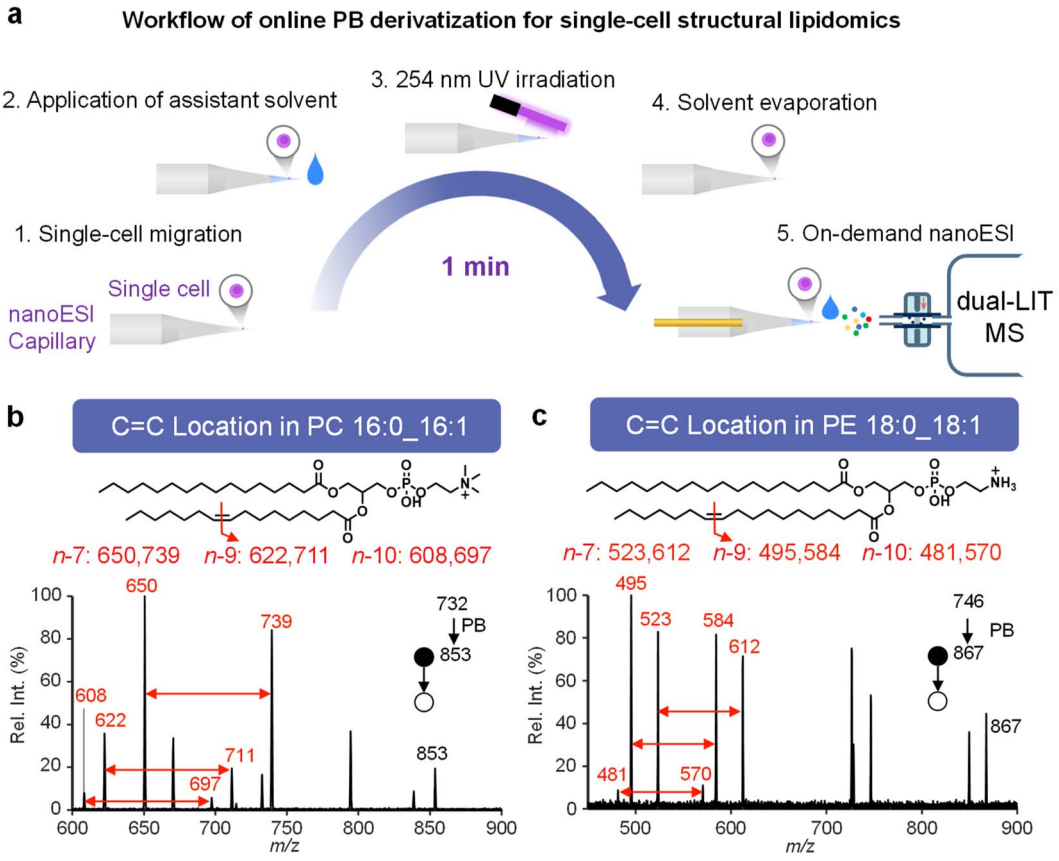

Fig. 3 Lipid structure identification at the level of C=C location for a single MDA-MB-468 cell. (a) Workflow of online photochemical derivatization. (b and c) MS/MS spectra of PB product to determine the lipid structure of (b) [^{PB}PC 16:0_16:1 + H]$^+$ (*m*/*z* 853) and (c) [^{PB}PE 18:0_18:1 + H]$^+$ (*m*/*z* 867). UV lamp: 254 nm, 5W.

a characteristic neutral loss of 185 Da. In total, 64 lipids were identified at the molecular sum composition level (Fig. S16 and Table S1), and 30 lipids were characterized at the C=C location level from a single MDA-MB-468 cell (Table S2), demonstrating the method's ability to analyze lipids with high coverage and C=C specificity. Of note, PCs and PEs are the primary lipids detected, and the lower detection of PS and SM species could be attributed to several factors, including their inherently lower ionization efficiency and the targeted analysis strategy, which prioritized ions based on pre-defined abundance thresholds.

sn-Position and C=C/*sn*-position specificity of lipid analysis

To achieve the ultimate lipid structural characterization for single-cell analysis, we implemented a strategy of combined MS^3/MS^4 analysis of sodiated PB products for the lipidome.[31] MS^3 analysis of these sodiated products releases *sn*-specific fatty acyls containing the 2-AP-derivatized C=C bond. Further MS^4 analysis allows C=C location determination in the *sn*-specific fatty acyl, avoiding ambiguities in the determination of C=C location and *sn*-positions of fatty acyls for phospholipids (Fig. 4a).

The PB-MS^3/MS^4 method requires a minimum of three MS^n analyses to fully elucidate the complete structure of a target phospholipid. To evaluate the performance of this strategy, we performed MS^3 analysis of mixed PC 16:0/18:1(*n*-9) and PC 18:1(*n*-9)/16:0 (Fig. S17), releasing *sn*-specific fatty acyls containing 2-AP derivatized C=C (*m*/*z* 380/396 and 466 for C18:1 at *sn*-2 and *sn*-1, respectively). MS^4 analysis of these *sn*-specific

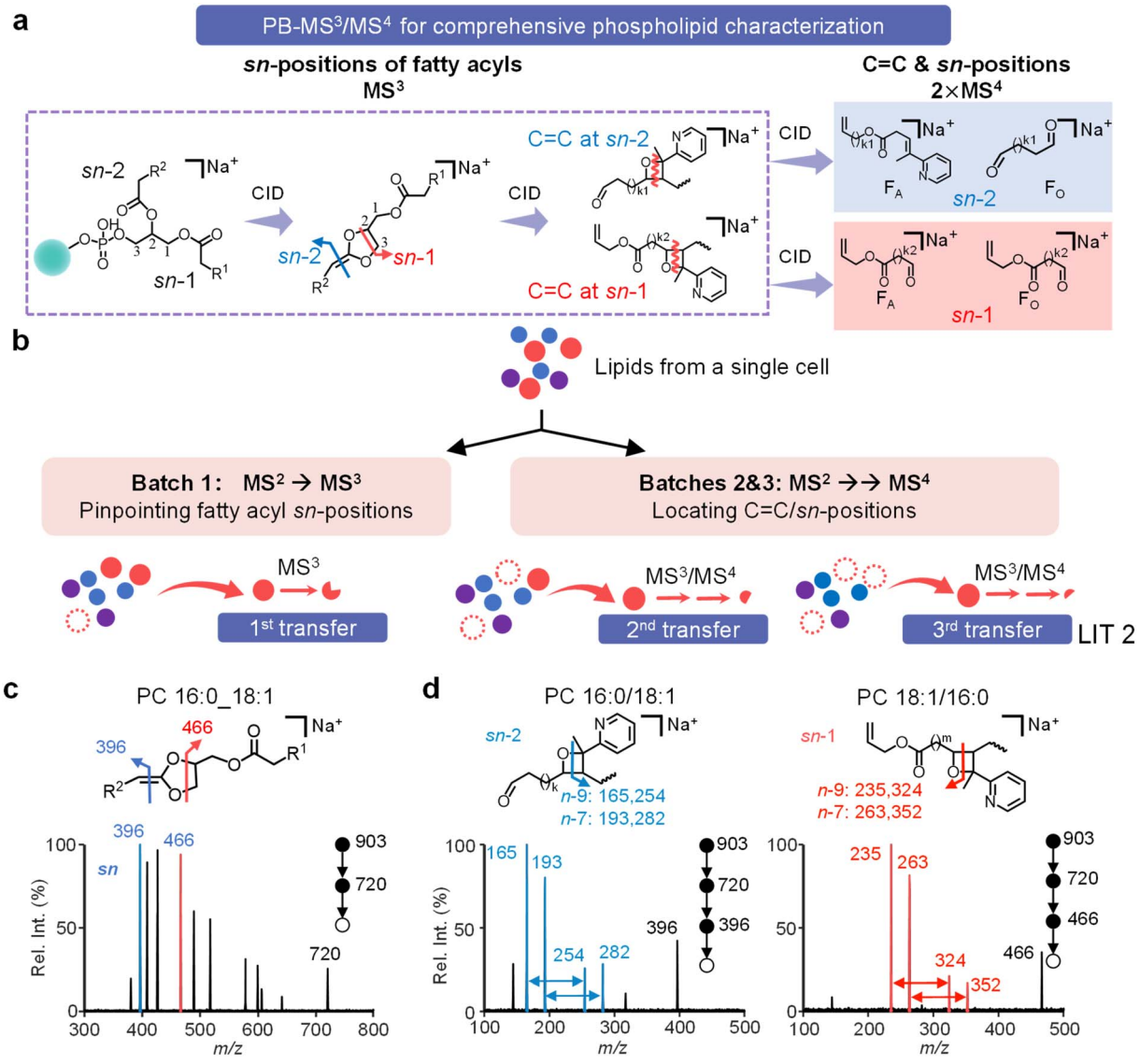

Fig. 4 Lipid structure identification at the level of *sn*-position of fatty acyl and C=C/*sn*-position for a single MDA-MB-468 cell. (a) PB-MS^3/MS^4 for comprehensive phospholipid characterization. (b) A schematic illustrating multiple transfers of targeted lipids from LIT 1 to LIT 2, and each subgroup of ions was separately analyzed *via* MS^3 or MS^4 to acquire different levels of lipid structure information. (c) Using the PC 16:0_18:1 ion to assign fatty acyl *sn*-positions, showing that PC 16:0_18:1 was a mixture of PC 16:0/18:1 (*m*/*z* 396) and 18:1/16:0 (*m*/*z* 466). PC 16:0/18:1 (R^1: $C_{14}H_{29}$, R^2: $C_{16}H_{31}$) or PC 18:1/16:0 (R^1: $C_{16}H_{31}$, R^2: $C_{14}H_{29}$). (d) Assigning C=C locations in PC 16:0/18:1 (*m*/*z* 396) and PC 18:1/16:0 (*m*/*z* 466). For C=C at the *n*-9 location, *k*: 5 and *m*: 7; for C=C at the *n*-7 location, *k*: 7 and *m*: 9.

fragments confirmed the C=C location within *sn*-1 and *sn*-2 C18:1 fatty acyl, both at the *n*-9 location.

Using conventional MS instrumentation, without ion accumulation, a lipid precursor can only sustain one round of MS/MS, posing a challenge for comprehensive lipid characterization that requires multiple rounds of MS^n analysis. The dual-LIT MS platform offers the flexibility to tackle this challenge *via* the MMPT mode, as shown in Fig. 1b. With the target lipid stored in LIT 1, MMPT enables partial transfers of these stored lipid ions to LIT 2 in a time sequence, enabling the detailed and complete MS^n analysis required for ultimate phospholipid identification, and *sn*-position and C=C location isomer quantitation in a single-cell lipidome. Operationally, derivatized lipids were transferred from LIT 1 to LIT 2 in three batches and subjected to one MS^3 and two MS^4 analyses (Fig. 4b).

To facilitate sodium-adduct formation, a spray solvent of methanol/acetonitrile (1 : 1, v/v), added to 100 μM sodium acetate, was used. Within LIT 1, 9 sodiated PB lipid products were accumulated after the removal of intact lipid ions in the low-mass range (Fig. S18). Five of the most abundant derivatized lipids, including ^{PB}PC 32:1 (*m*/*z* 875), ^{PB}PC 34:2 (*m*/*z* 901), ^{PB}PC 34:1 (*m*/*z* 903), ^{PB}PC 36:2 (*m*/*z* 929), and ^{PB}PC 36:1 (*m*/*z* 931), were subjected to MS^n analyses (one MS^3 and two MS^4) *via* MMPT. The remaining four lipids were analyzed by PB-MS^3 for the determination of *sn*-positions of fatty acyls. Analysis of all these lipid products in an MDA-MB-468 cell was completed within approximately 25 s.

MS^3 analysis of ^{PB}PC 34:1 (*m*/*z* 903) identified it as a mixture of PC 16:0/18:1 (*m*/*z* 396) and PC 18:1/16:0 (*m*/*z* 466) (Fig. 4c). The MS^3 spectra of the other eight lipids are shown in Fig. S19. Subsequent MS^4 analyses of the *sn*-specific fatty acyls (*m*/*z* 396, 466) showed the C18:1 fatty acyl at the *sn*-1 and *sn*-2 positions to be a mixture of *n*-9 and *n*-7 isomers, as evidenced by the corresponding pairs of diagnostic ions (highlighted in red in Fig. 4d). Our method revealed PC 16:0/18:1 to be composed of four distinct isomers in MDA-MB-468 cells, *i.e.*, PC 16:0/18:1(*n*-9), PC 16:0/18:1(*n*-7), PC 18:1(*n*-9)/16:0, and PC 18:1(*n*-7)/16:0. These findings strongly support the method's capability for unprecedented single-cell lipidome analysis with high structural specificity.

Multi-dimensional in-depth single-cell lipidome characterization

The technique enables comprehensive lipid characterization at the single-cell level, encompassing lipid sum compositions, C=C locations, *sn*-positions of fatty acyls, and C=C/*sn*-positions. Three rounds of sampling from a single cell were required for this comprehensive analysis. The first two rounds of sampling focused on determining lipid sum compositions and C=C locations. The third round of sampling was dedicated to identifying the *sn*-position and C=C/*sn*-position. From a single MDA-MB-468 cell, we successfully identified 64 molecular lipids (35 PCs, 20 PEs, 8 PSs, and 1 SM), 30 lipid C=C location isomers, and 23 lipid *sn*-position isomers (Table S3). Furthermore, 20 distinct lipids were characterized at C=C/*sn*-position levels (Table S4).

Excluding duplicated lipids, a total of 55 lipids were identified at the lipid sum composition level, with 16 identified at the C=C location level, 10 lipids identified at the *sn*-position level, and 24 identified at the combined C=C/*sn*-position level. In particular, a total of 8 isomers were identified for PC 34:2, including two isomers at the *sn*-position level (PC 16:0/18:2 (*n*-6, 9), and PC 18:2 (*n*-6, 9)/16:0) and six isomers at the C=C/*sn*-position level (PC 16:1/18:1(*n*-7), PC 16:1/18:1(*n*-9), PC 18:1(*n*-7)/16:1, and PC 18:1(*n*-9)/16:1, PC 16:1/18:1(*n*-10), and PC 18:1(*n*-10)/16:1). These findings demonstrate the remarkable depth of lipid structural information that can be obtained from a single cell using our developed method.

This single-cell lipidomics method was successfully applied to MCF-7 and BT-474 cell lines, and the identification results are summarized in Tables S5–10. A total of 60 molecular lipid species, 28 lipid C=C location isomers, 21 lipid *sn*-position isomers, and 20 lipid C=C/*sn*-position isomers were detected for MCF-7 cells. For BT-474 cells, a total of 56 molecular lipid species, 23 lipid C=C location isomers, 18 lipid *sn*-position isomers, and 20 lipid C=C/*sn*-position isomers were detected (Fig. S20). Distinct lipid profiles were acquired and can be used for the accurate grouping of MDA-MB-468, MCF-7, and BT-474 cells. Of note, the number of different lipids with structural specificity identified from a human breast cancer cell is higher than that which can be obtained with existing methods.[27–29,40,41]

The quantification of lipid isomers in this study is based on the relative intensities of their diagnostic ions. This approach assumes that the ionization efficiencies of isomers derived from the same parent ion are comparable, and that diagnostic ions for different isomers are generated with similar fragmentation efficiencies. While these assumptions are necessary for relative quantification at the single-cell level, we acknowledge that they could be influenced by factors such as differential fragmentation or ion trap residence times. However, the high structural similarity of isomers, particularly for C=C location isomers, suggests that these effects are likely minor. The consistency of our isomer ratio data with that in the existing literature further supports the validity of this quantitative approach.

In an ideal scenario, quantification could be achieved by spiking a known amount of an internal standard into a single cell. However, due to the extremely small volume of a single cell (<pL), it remains technically challenging to accurately introduce such a minute quantity. For the derivatization step, reproducibility at the single-cell level is achievable because the reaction is relatively stable. Quantification was achieved by normalizing lipid signals to either mutual internal standards (for C=C isomers with similar efficiencies) or a single intense benchmark peak (*e.g.*, *m*/*z* 760 for PC 34:1). Therefore, to ensure robust reproducibility, several strategies can be employed: applying internal calibration standards for signal correction; developing optimized normalization protocols, such as those utilizing stable isotope-labeled or endogenous housekeeping lipids, to correct for cell-to-cell heterogeneity; and integrating real-time monitoring systems for immediate quality assurance.

In addition to comprehensive single-cell lipidome analysis including lipid isomers, we next aimed to evaluate the performance of our method with respect to quantitative analysis of

lipid isomers (C=C location, *sn*-position). Fig. 5a shows the distribution of C=C location isomers (*n*-7, *n*-9, and *n*-10) for phospholipids containing a C18:1 and C16:1 fatty acyl. Notably, the proportion of C18:1 (*n*-7) is greater than 80% (calculated using identities of diagnostic ions) in PC 16:1_18:1. By comparison, in PC 16:0_18:1, the relative amount of C18:1 (*n*-7) was only approximately 50%. Due to the high structure-resolving power of our method, we can even acquire the isomer composition of C16:1 or C18:1 in an *sn*-specific approach. The different *sn*-position of C16:1 or C18:1 fatty acyl does not seem to affect its C=C isomer compositions (Fig. 5b). A significant advantage of isomer analysis is its low coefficient of variation (CV). This may stem from the similar ionization and fragmentation efficiencies of the isomers and the fact that fluctuations in these efficiencies between individual cells are cancelled out through ratio calculation. This implies that more reproducible quantitative data for single-cell analysis can be obtained *via* ratio-based normalization, thereby achieving better quality control and laying a solid foundation for subsequent applied research.

Fig. 5c illustrates the *sn*-position isomer composition of representative phospholipids with fatty acyls identified. For example, PC 34:2 is a mixture of two pairs of *sn*-isomers: PC 16:1/18:1, PC 18:1/16:1, PC 16:0/18:2, and PC 18:2/16:0. These results are consistent with existing studies and confirm the robustness of the method for qualitative and quantitative analysis at the single-cell lipidome level.[31]

Distinguishing DOX-resistant and DOX-sensitive CML K562 cells

DOX is a widely utilized, broad-spectrum anti-tumor agent in leukemia therapy. Despite initial treatment efficacy, some patients can develop acquired DOX resistance. Accurate differentiation between DOX-resistant and -sensitive K562 cells in heterogeneous populations is crucial. Although there is sufficient evidence that DOX resistance is closely related to membrane proteins,[42,43] insufficient research has been conducted on the cellular lipidome.[44] In this section, we aim to differentiate DOX-resistant and DOX-sensitive CML K562 cells by analyzing their lipidomes at the single-cell level. DOX-resistant K562 cells were developed through prolonged exposure to 1 μg mL^{-1} DOX over 20 passages, while wild-type K562 cells, which were DOX-sensitive, served as controls.

A targeted lipidomics analysis focused on 24 high-abundance and 20 low-abundance lipids. A total of 30 PCs, 14 PEs, and 8 PSs were detected at the sum composition level (Table S11), along with 30 C=C location isomers and 23 *sn*-position isomers (Tables S12 and S13). The lipid C=C location and *sn*-position isomers were expressed as isomer ratios to improve data robustness and quantitative accuracy (Table S14).[41] The resulting dataset, *i.e.*, a total of 96 dimensions including 51 lipid sum compositions (excluding PC 34:1), 22 C=C locations, 13 *sn*-positions, and 10 C=C/*sn*-positions, was used for comparative analysis.

The *t*-distributed stochastic neighbor embedding (*t*-SNE) algorithm and *k*-means method were employed to cluster DOX-

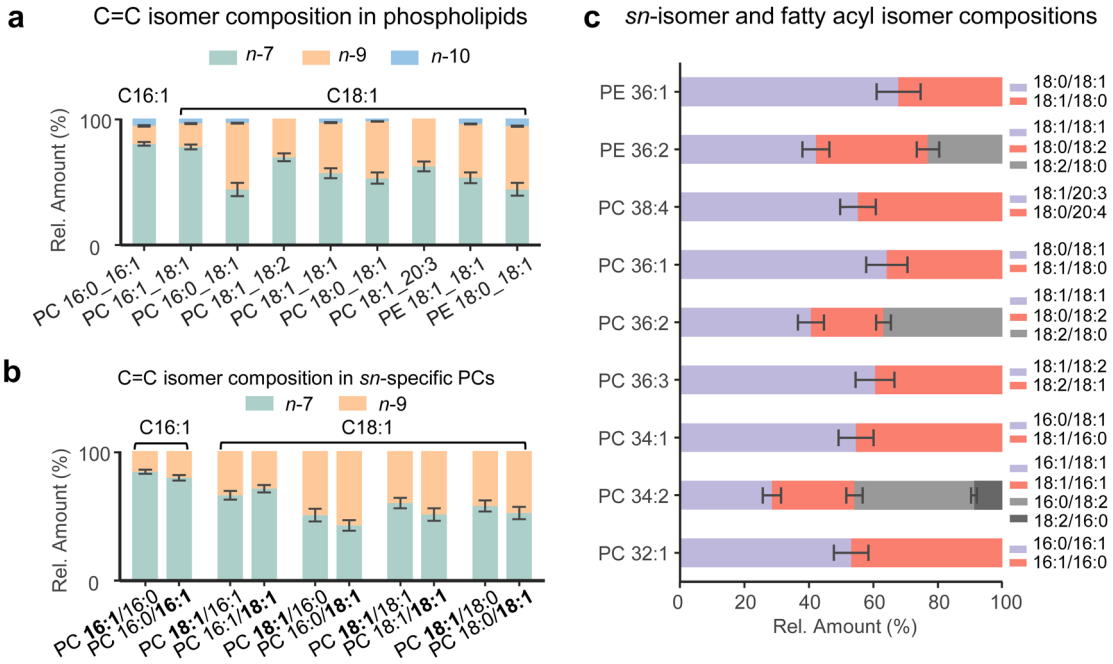

Fig. 5 In-depth lipid profiling of single MDA-MB-468 cells ($N = 10$) using photochemical lipid derivatization and a dual-LIT mass spectrometer. (a) Isomeric composition of C18:1- or C16:1-containing phospholipids: *n*-7, *n*-9 and *n*-10. (b) Composition of C=C isomers from specific *sn*-positions (C=C/*sn*-positions) *via* PB-MS^4 analysis-derivatized PCs from single MDA-MB-467 cells. The relative amount was calculated by the intensity of the C=C-specific diagnostic ions for a specific isomer divided by the total intensity of those for all possible C=C isomers. (c) Composition of phospholipid *sn*-position isomers for PCs and PEs. The relative amount was calculated by the intensity of the *sn*-position specific diagnostic ions for a specific isomer divided by the total intensity of those for all possible *sn*-position isomers.

resistant and -sensitive cells. To assess the effectiveness of different lipid features for distinguishing cell types, clustering analyses were conducted using various factors, including lipid sum composition, C=C location, *sn*-position, and their combinations (Fig. 6a and S22). Lipid composition alone failed to accurately discriminate the two cell types, with approximately 50% overlap between the two clusters. By comparison, it was found that the C=C location is a highly discriminating feature, highlighting the importance of single-cell structural lipidomics in biological applications. With multiple lipidomic features available, it can be expected that their combination could further improve the accuracy of cell classification.

Cluster 1 was tentatively identified as DOX-resistant cells, with Cluster 2 identified as DOX-sensitive cells. Across all analyses shown in Fig. 5a, three cells are consistently misclassified (Fig. 5a and S22a–c). Specifically, cell #8(C1), a DOX-resistant cell, was incorrectly classified as DOX-sensitive, and cells #33(C2) and #38(C3), both DOX-sensitive, were misclassified as DOX-resistant. This resulted in an overall classification accuracy of 94.9%. The discrepancy of C2 and C3 cells might be attributed to the presence of drug-resistant subpopulations in the DOX-sensitive cells, aligning with the known existence of a small proportion of DOX-resistant cells within the otherwise sensitive populations.[45]

Lipidomic analysis of the remaining cell populations, excluding misclassified cells, revealed significant differences in lipid classes, C=C locations, *sn*-positions, and C=C locations at specific *sn*-positions (Fig. 6b). Volcano plot analysis identified 20 lipid features that are most significant to discriminate DOX-resistant and -sensitive cells ($p < 10^{-5}$), including four molecular lipid species, seven lipid C=C location isomers, five *sn*-position isomers, and four C=C location isomers with identified fatty acyl *sn*-positions (Fig. S23 and S24). For example, the *n*-10/*n*-7 isomer ratio of PC 16:0_16:1 was reduced mainly in DOX-resistant K562 cells (Fig. 6c), and the PE 18:1/18:1 to PE 18:2/18:0 ratio for PE 36:2 was also lower in DOX-resistant cells (Fig. 6c). Conversely, the C18:1 *n*-9/*n*-7 ratio for PC 16:1/18:1 was much higher in DOX-resistant cells (Fig. 6c). While the biological implications of these lipidome changes require further investigation, this study demonstrates that our single-cell lipidomics method is a powerful tool for analyzing cellular lipid heterogeneity and evaluating the drug resistance of cancer cells.

Variations in the cellular lipidome at multiple structural levels during ferroptosis

Ferroptosis is emerging as a critical factor in cancer, offering a potential therapeutic target for inducing cancer cell death and insights into the mechanisms of tumor suppression and chemoresistance.[46–49] Ferroptosis can be triggered by inhibiting glutathione peroxidase 4 (GPX4) with small-molecule compounds, leading to lipid peroxidation through the accumulation of reactive oxygen species.[50,51] While the link between

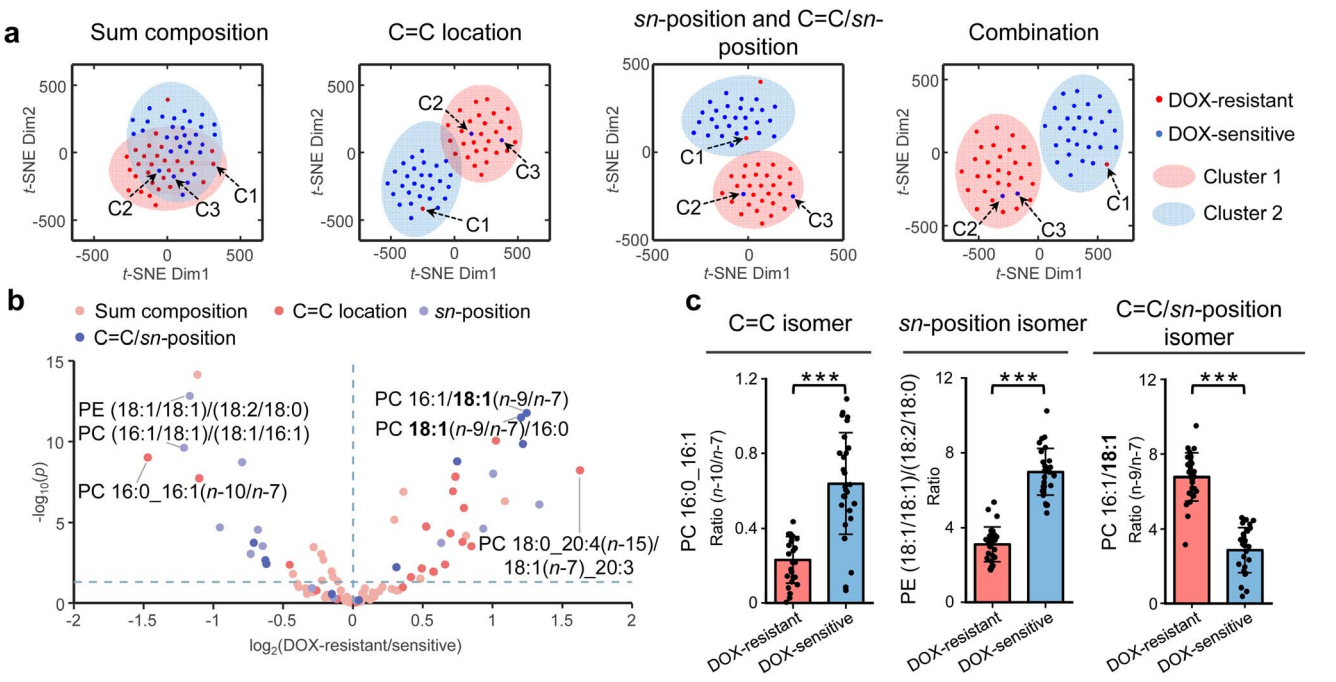

Fig. 6 Discrimination of DOX-resistant ($N = 29$) and DOX-sensitive ($N = 30$) human chronic myelogenous leukemia K562 cells. (a) *t*-SNE plot of DOX-resistant group cells and DOX-sensitive group cells by lipid composition, ratio of different C=C location isomers, ratio of *sn*-position isomers and C=C/*sn*-position isomers, and combination (lipid composition, ratio of C=C location isomers, ratio of different *sn*-position isomers, and ratio of C=C/*sn*-position isomers). Two cluster areas were circled by *k*-means clustering results with a confidence probability of 0.95. C1 was cell #8, C2 was cell #33, and C3 was cell #38. (b and c) DOX-resistant ($N = 28$) and DOX-sensitive ($N = 28$). (b) Alterations of lipids, the ratio of C=C location isomers, the ratio of different *sn*-position isomers, and the ratio of C=C/*sn*-position isomers. (c) Comparison of the ratio (*n*-10)/(*n*-7) of PC 16:0_16:1, PE (18:1/18:1)/(18:2/18:0) and PC 16:1/18:1(*n*-9/*n*-7) between DOX-resistant group cells and DOX-sensitive group cells. ***: $p < 0.001$. *P*-values were determined by a two-tailed *t*-test. Error bars represent standard deviations (SDs).

lipid peroxidation and ferroptosis is well established, the connection between ferroptosis and lipid remodeling remains to be explored at the structural lipidomics level, *e.g.*, at C=C location and *sn*-position levels. For this purpose, we induced ferroptosis in multiple cancer cell lines (MDA-MB-468, MCF-7, BT-474, and HepG2) using erastin, a highly potent ferroptosis inducer (Fig. 7a). Lipid species identified from HepG2 are shown in Tables S15–S17. The single-cell lipidomics data are subjected to data conversion, previously used for the analysis of K562 cells, for comparative analysis (Fig. 7b).

Among all four cell lines after ferroptosis induction, HepG2 cells exhibited the most pronounced ferroptotic response, as evidenced by the significant alterations in single-cell lipidome profiles. *t*-SNE classification of the single-cell lipid data for the HepG2 cell population revealed distinct clustering patterns before and after ferroptosis (Fig. 7c). By contrast, BT-474 and MCF-7 cells were relatively insensitive to ferroptosis (Fig. 7c and S26). MDA-MB-468 cells were sensitive to ferroptosis, but the two cell clusters overlapped (Fig. 7c). These findings aligned with those of previous studies (Fig. S25).[52] Hierarchical clustering of MDA-MB-468, performed without a pre-set number of classes, identified three cell groups: control, ferroptosis, and a transition group in the overlapped regions (Fig. S27). The transition group included nine cells from the ferroptosis group and six from the control group. Re-clustering confirmed the transition group to be intermediate between the control and ferroptosis groups (Fig. S28).

Upon further re-hierarchical clustering (Fig. 7d), it was observed that PE 38:4 levels were significantly lower in the ferroptosis group compared to the control, but similar to those in the transition group (Fig. 7e). This is consistent with the fact that PE 38:4 (*i.e.*, PE 18:0_20:4) is depleted by lipid peroxidation during ferroptosis.[50] The significantly higher ratio of PC (18:1/18:3)/(16:0/20:4) in the ferroptosis group is also consistent with C20:4 depletion (Fig. 7f). We also noted lipid changes at the C=C level. For instance, in PE 18:1_18:1, the *n*-10/*n*-7 ratio was higher in the ferroptosis and transition groups than in the control group, possibly suggesting a relatively higher activity of fatty acid desaturase 2 (FADS2) (Fig. 7g). Elevated levels of C18:1 *n*-9/*n*-7 ratios were also observed in multiple lipid species, suggesting an altered interplay between stearoyl-CoA desaturase 1 (SCD1) and β oxidation.[53,54]

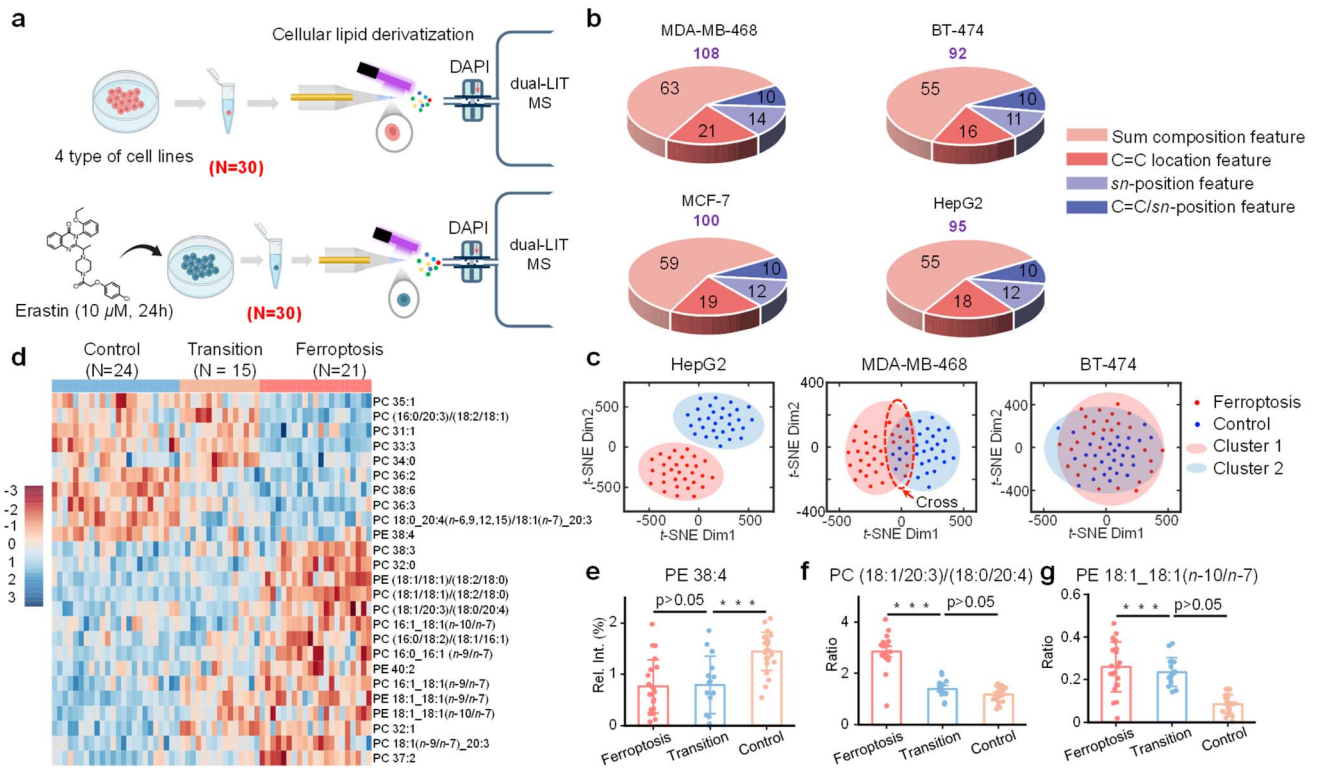

Fig. 7 Results of ferroptosis induction in single cells, including HepG2, MDA-MB-468, and BT-474. Control group (DMSO), ferroptosis-induced group (10 μmol erastin, 24 h). (a) Schematic diagram of the cell culture process. (b) The number of features quantified at different levels for different cell lines. (c) *t*-SNE plot using MS/MS analysis results, including lipid sum composition, the ratio of C=C location isomers, the ratio of different *sn*-position isomers, and the ratio of C=C/*sn*-position isomers. Ferroptosis-induced group cells ($N = 30$) and control group cells ($N = 30$) of HepG2, MDA-MB-468 and BT-474. Two cluster areas were circled by k-means clustering results with a confidence probability of 0.95. (d–g) MDA-MB-468. (d) Hierarchical cluster analysis of ferroptosis-induced group cells, cells in the transition state, and control group cells. The top 25 features ranked by −log(*p*) values were used for the cluster. (e–g) Comparison among ferroptosis-induced group cells, cells in the transition state, and control group cells of (e) the relative intensity of PE 38:4 (normalized to intensity of PC 34:1), (f) the ratio of PC (18:1/20:3)/(18:0/20:4), and (g) the ratio of PE 18:1_18:1(*n*-10/*n*-7). *: $p < 0.01$; **: $p < 0.005$; ***: $p < 0.001$. *P*-values were determined by a two-tailed *t*-test. Error bars represent SDs.

The transition group cells, which accounted for 25% of the total cell population, might represent a state of ferroptosis resistance. This ratio was consistent with those reported in previous studies on ferroptosis sensitivity in various cell populations.[52] The distinct 'Transition' state may represent the asynchronous onset of ferroptosis, where cells initiate lipid peroxidation at different times. This is reflected in the heterogeneous lipidome profile (Fig. 7d–g), a mixture of cells depleting susceptible lipids (such as PE 38:4) alongside those that have not. Furthermore, this state could involve alternative lipid remodeling pathways. This transitional population, resisting full ferroptotic commitment, is analogous to partial drug resistance, linking our findings to broader cellular stress responses.

Conclusion

Lipidomics analyses of bulk samples have achieved significant developments, identifying over 1000 lipid species at the level of sum compositions, C=C location, and *sn*-position.[55,56] However, single-cell lipidomics faces unique challenges. Limited sample content from single mammalian cells restricts the number of feasible MS/MS analyses, and low ion utilization poses significant obstacles to comprehensive lipid structural characterization and accurate quantitative analysis. To address these limitations, we developed a high-coverage single-cell structural lipidomics method utilizing dual-LIT MS coupled with single-cell electrospray technology and online photochemical derivatization. The dual-LIT MS system, with its efficient ion storage capabilities, maximizes ion utilization and offers versatile MS^n capabilities crucial for comprehensive lipid structure characterization.

Overall, this method represents a significant advancement and innovation in several aspects. (1) Enhanced ion utilization and MS^n capabilities: the current study focuses on significantly improving ion utilization efficiency and expanding the capabilities of MS^n analysis. We optimized the dual-LIT MS system, particularly the vacuum regulation system, to achieve efficient ion storage for over 30 s with minimal ion loss. This enhancement allows for multiple rounds of MS^n analysis (n = 2–4) for each lipid species, enabling comprehensive structural characterization at different levels. We also implemented a PB-MS^3/MS^4 analysis strategy for comprehensive phospholipid characterization. This approach enables the determination of *sn*-specific fatty acyls and C=C locations within them, providing the most in-depth analysis of phospholipids within single cells to date. (2) Targeted lipidomics strategy for high coverage: we developed a targeted lipidomics strategy to overcome the challenges of ion interference and maximize the coverage of lipid species within single cells. This strategy involves the separate analysis of high- and low-abundance lipid ions, using the MMPT mode for low-abundance ions and separate ion injection for high-abundance ions. This approach significantly improves the dynamic range of detectable lipids and enables the identification of 100+ distinct lipid molecules from a single cell. (3) Application to cell drug resistance and ferroptosis: we successfully applied the developed method to distinguish between DOX-resistant and DOX-sensitive K562 cells with high accuracy and to investigate ferroptosis in multiple cancer cell lines. These applications demonstrate the significant potential of this novel single-cell structural lipidomics method for advancing research on cell drug resistance and programmed cell death. In summary, we anticipate that this technology will have broad prospects for advancing deep single-cell lipidomic analysis and its applications.

Conflicts of interest

The authors declare the following competing financial interest(s): Zheng Ouyang is the founder of PURSPEC Technologies Inc., which develops miniature mass spectrometry systems.

Data availability

The data supporting this article have been included as part of the supplementary information (SI). Supplementary information: the single-cell experiment procedure, modes of ion manipulation *via* the dual-LIT-MS, single cell lipidome analysis *via* PB reactions, and lists of lipids identified. See DOI: https://doi.org/10.1039/d5sc08665e.

Acknowledgements

This work was supported by the Beijing Natural Science Foundation (Grant: 2232007), the National Key R&D Program of China (Grant: 2022YFC3401900), and the National Natural Science Foundation of China (Grants: 21934003 and 22574092).

References

1 S. J. Altschuler and L. F. Wu, *Cell*, 2010, **141**, 559–563.
2 D. G. Spiller, C. D. Wood, D. A. Rand and M. R. White, *Nature*, 2010, **465**, 736–745.
3 F. A. Rosenberger, M. Thielert and M. Mann, *Nat. Methods*, 2023, **20**, 320–323.
4 T. Wälchli, M. Ghobrial, M. Schwab, S. Takada, H. Zhong, S. Suntharalingham, S. Vetiska, D. R. Gonzalez, R. Wu, H. Rehrauer, A. Dinesh, K. Yu, E. L. Y. Chen, J. Bisschop, F. Farnhammer, A. Mansur, J. Kalucka, I. Tirosh, L. Regli, K. Schaller, K. Frei, T. Ketela, M. Bernstein, P. Kongkham, P. Carmeliet, T. Valiante, P. B. Dirks, M. L. Suva, G. Zadeh, V. Tabar, R. Schlapbach, H. W. Jackson, K. De Bock, J. E. Fish, P. P. Monnier, G. D. Bader and I. Radovanovic, *Nature*, 2024, **632**, 603–613.
5 A. J. Ibanez, S. R. Fagerer, A. M. Schmidt, P. L. Urban, K. Jefimovs, P. Geiger, R. Dechant, M. Heinemann and R. Zenobi, *Proc. Natl. Acad. Sci. U. S. A.*, 2013, **110**, 8790–8794.
6 R. Zenobi, *Science*, 2013, **342**, 1243259.
7 C. Seydel, *Nat. Methods*, 2021, **18**, 1452–1456.
8 H. Zhu, Q. Li, T. Liao, X. Yin, Q. Chen, Z. Wang, M. Dai, L. Yi, S. Ge, C. Miao, W. Zeng, L. Qu, Z. Ju, G. Huang, C. Cang and W. Xiong, *Nat. Methods*, 2021, **18**, 788–798.
9 A. Ali, S. Davidson, E. Fraenkel, I. Gilmore, T. Hankemeier, J. A. Kirwan, A. N. Lane, I. Lanekoff, M. Larion,

L. I. McCall, M. Murphy, J. V. Sweedler and C. Zhu, *Metabolomics*, 2022, **18**, 77.
10 Q. Zhang, Y. Tamura, M. Roy, Y. Adachi, M. Iijima and H. Sesaki, *Cell. Mol. Life Sci.*, 2014, **71**, 3767–3778.
11 E. Sezgin, I. Levental, S. Mayor and C. Eggeling, *Nat. Rev. Mol. Cell Biol.*, 2017, **18**, 361–374.
12 E. M. Storck, C. Özbalci and U. S. Eggert, *Annu. Rev. Biochem.*, 2018, **87**, 839–869.
13 Q. Liu, W. Ge, T. Wang, J. Lan, S. Martinez-Jarquin, C. Wolfrum, M. Stoffel and R. Zenobi, *Angew. Chem., Int. Ed.*, 2021, **60**, 24534–24542.
14 T. Xu, H. Li, P. Dou, Y. Luo, S. Pu, H. Mu, Z. Zhang, D. Feng, X. Hu, T. Wang, G. Tan, C. Chen, H. Li, X. Shi, C. Hu and G. Xu, *Adv. Sci.*, 2024, **11**, e2306659.
15 X. Zhao, J. Liang, Z. Chen, R. Jian, Y. Qian, Y. Wang, Z. Guo, W. Zhang, Y. Zhang, H. Yin and Y. Xia, *Angew. Chem., Int. Ed.*, 2023, **62**, e202215556.
16 J. P. Menzel, R. S. E. Young, A. H. Benfield, J. S. Scott, P. Wongsomboon, L. Cudlman, J. Cvacka, L. M. Butler, S. T. Henriques, B. L. J. Poad and S. J. Blanksby, *Nat. Commun.*, 2023, **14**, 3940.
17 T. J. Gu, P. K. Liu, Y. W. Wang, M. T. Flowers, S. Xu, Y. Liu, D. B. Davis and L. Li, *Nat. Chem.*, 2024, **16**, 762–770.
18 G. Feng, M. Gao, L. Wang, J. Chen, M. Hou, Q. Wan, Y. Lin, G. Xu, X. Qi and S. Chen, *Nat. Commun.*, 2022, **13**, 2652.
19 S. Tang, H. Wang, H. Zhang, M. Zhang, J. Xu, C. Yang, X. Chen and X. Guo, *J. Am. Chem. Soc.*, 2024, **146**, 29503–29512.
20 X. Ma, L. Chong, R. Tian, R. Shi, T. Y. Hu, Z. Ouyang and Y. Xia, *Proc. Natl. Acad. Sci. U. S. A.*, 2016, **113**, 2573–2578.
21 P. Morigny, J. Boucher, P. Arner and D. Langin, *Nat. Rev. Endocrinol.*, 2021, **17**, 276–295.
22 S. Cheng, D. Zhang, J. Feng, Q. Hu, A. Tan, Z. Xie, Q. Chen, H. Huang, Y. Wei, Z. Ouyang and X. Ma, *Research*, 2023, **6**, 0087.
23 A. S. Mutlu, J. Duffy and M. C. Wang, *Dev. Cell*, 2021, **56**, 1394–1407.
24 S. A. Lim, W. Su, N. M. Chapman and H. Chi, *Nat. Chem. Biol.*, 2022, **18**, 470–481.
25 S. Oh, C. Lee, W. Yang, A. Li, A. Mukherjee, M. Basan, C. Ran, W. Yin, C. J. Tabin, D. Fu, X. S. Xie and M. W. Kirschner, *Proc. Natl. Acad. Sci. U. S. A.*, 2022, **119**, e2117938119.
26 S. N. Thomas, D. French, P. J. Jannetto, B. A. Rappold and W. A. Clarke, *Nat. Rev. Methods Primers*, 2022, **2**, 96.
27 S. Qin, Y. Zhang, M. Shi, D. Miao, J. Lu, L. Wen and Y. Bai, *Nat. Commun.*, 2024, **15**, 350.
28 H. Zhang, Y. Liu, L. Fields, X. Shi, P. Huang, H. Lu, A. J. Schneider, X. Tang, L. Puglielli, N. V. Welham and L. Li, *Nat. Commun.*, 2023, **14**, 5185.
29 Z. Li, S. Cheng, Q. Lin, W. Cao, J. Yang, M. Zhang, A. Shen, W. Zhang, Y. Xia, X. Ma and Z. Ouyang, *Nat. Commun.*, 2021, **12**, 2869.
30 M. R. L. Paine, B. L. J. Poad, G. B. Eijkel, D. L. Marshall, S. J. Blanksby, R. M. A. Heeren and S. R. Ellis, *Angew. Chem., Int. Ed.*, 2018, **57**, 10530–10534.
31 W. Cao, S. Cheng, J. Yang, J. Feng, W. Zhang, Z. Li, Q. Chen, Y. Xia, Z. Ouyang and X. Ma, *Nat. Commun.*, 2020, **11**, 375.
32 X. Liu, X. Wang, J. Bu, X. Zhou and Z. Ouyang, *Anal. Chem.*, 2019, **91**, 1391–1398.
33 X. Guo, W. Cao, X. Fan, Z. Guo, D. Zhang, H. Zhang, X. Ma, J. Dong, Y. Wang, W. Zhang and Z. Ouyang, *Angew. Chem., Int. Ed.*, 2022, e202214804, DOI: 10.1002/anie.202214804.
34 X. C. Zhang, Z. W. Wei, X. Y. Gong, X. Y. Si, Y. Y. Zhao, C. D. Yang, S. C. Zhang and X. R. Zhang, *Sci. Rep.*, 2016, **6**, 24730.
35 Y. Cong, K. Motamedchaboki, S. A. Misal, Y. Liang, A. J. Guise, T. Truong, R. Huguet, E. D. Plowey, Y. Zhu, D. Lopez-Ferrer and R. T. Kelly, *Chem. Sci.*, 2021, **12**, 1001–1006.
36 P. Mandal, S. Das, D. De Munshi, T. Dutta and M. Mukherjee, *Int. J. Mass Spectrom.*, 2014, **364**, 16–20.
37 N. Li, X. Zhou and Z. Ouyang, *Int. J. Mass Spectrom.*, 2021, **462**, 116523.
38 M. H. Soni and R. G. Cooks, *Anal. Chem.*, 1994, **66**, 2488–2496.
39 Z. Xu, T. Jiang, Q. Xu, Y. Zhai, D. Li and W. Xu, *Anal. Chem.*, 2019, **91**, 13838–13846.
40 Y. Zhu, W. Wang and Z. Yang, *Anal. Chem.*, 2020, **92**, 11380–11387.
41 S. Cheng, C. Cao, Y. Qian, H. Yao, X. Gong, X. Dai, Z. Ouyang and X. Ma, *Chem. Sci.*, 2024, **15**, 6314–6320.
42 H. Hamada and T. Tsuruo, *Cancer Res.*, 1988, **48**, 4926–4932.
43 M. Szwed, K. D. Kania and Z. Jozwiak, *Cell. Oncol.*, 2014, **37**, 421–428.
44 T. C. Karagiannis, M. Wall, K. Ververis, E. Pitsillou, S. M. Tortorella, P. A. Wood, H. Rafehi, I. Khurana, S. S. Maxwell, A. Hung, J. Vongsvivut and A. El-Osta, *Cell. Mol. Life Sci.*, 2023, **80**, 248.
45 S. Zhang, X. Liu, T. Bawa-Khalfe, L. S. Lu, Y. L. Lyu, L. F. Liu and E. T. Yeh, *Nat. Med.*, 2012, **18**, 1639–1642.
46 J. D. Scott, K. M. Lemberg, M. R. Lamprecht, R. Skouta, E. M. Zaitsev, C. E. Gleason, D. N. Patel, A. J. Bauer, A. M. Cantley, W. S. Yang, B. Morrison and B. R. Stockwell, *Cell*, 2012, **149**, 1060–1072.
47 J. P. Friedmann Angeli, D. V. Krysko and M. Conrad, *Nat. Rev. Cancer*, 2019, **19**, 405–414.
48 X. Jiang, B. R. Stockwell and M. Conrad, *Nat. Rev. Mol. Cell Biol.*, 2021, **22**, 266–282.
49 S. J. Dixon and J. A. Olzmann, *Nat. Rev. Mol. Cell Biol.*, 2024, **25**, 424–442.
50 S. Doll, B. Proneth, Y. Y. Tyurina, E. Panzilius, S. Kobayashi, I. Ingold, M. Irmler, J. Beckers, M. Aichler, A. Walch, H. Prokisch, D. Trumbach, G. Mao, F. Qu, H. Bayir, J. Fullekrug, C. H. Scheel, W. Wurst, J. A. Schick, V. E. Kagan, J. P. Angeli and M. Conrad, *Nat. Chem. Biol.*, 2017, **13**, 91–98.
51 D. Tang, X. Chen, R. Kang and G. Kroemer, *Cell Res.*, 2021, **31**, 107–125.
52 B. Seashore-Ludlow, M. G. Rees, J. H. Cheah, M. Cokol, E. V. Price, M. E. Coletti, V. Jones, N. E. Bodycombe, C. K. Soule, J. Gould, B. Alexander, A. Li, P. Montgomery, M. J. Wawer, N. Kuru, J. D. Kotz, C. S. Hon, B. Munoz, T. Liefeld, V. Dancik, J. A. Bittker, M. Palmer, J. E. Bradner,

A. F. Shamji, P. A. Clemons and S. L. Schreiber, *Cancer Discovery*, 2015, **5**, 1210–1223.

53 B. Koletzko, E. Reischl, C. Tanjung, I. Gonzalez-Casanova, U. Ramakrishnan, S. Meldrum, K. Simmer, J. Heinrich and H. Demmelmair, *Annu. Rev. Nutr.*, 2019, **39**, 21–44.

54 R. S. E. Young, A. P. Bowman, E. D. Williams, K. D. Tousignant, C. L. Bidgood, V. R. Narreddula, R. Gupta, D. L. Marshall, B. L. J. Poad, C. C. Nelson, S. R. Ellis, R. M. A. Heeren, M. C. Sadowski and S. J. Blanksby, *Cell Rep.*, 2021, **34**, 108738.

55 T. Xia, F. Zhou, D. Zhang, X. Jin, H. Shi, H. Yin, Y. Gong and Y. Xia, *Nat. Commun.*, 2023, **14**, 4263.

56 J. A. Michael, R. S. E. Young, R. Balez, L. J. Jekimovs, D. L. Marshall, B. L. J. Poad, T. W. Mitchell, S. J. Blanksby, C. S. Ejsing and S. R. Ellis, *Angew. Chem., Int. Ed.*, 2024, e202316793.